Int. J. Heat Mass Transfer. Vol. 36, No. 5, pp. 1171–1179, 1993
Printed in Great Britain

0017-9310/93 $6.00 + 0.00

Contact melting during sliding on ice

A. J. FOWLER and A. BEJAN
Department of Mechanical Engineering and Materials Science,
Duke University, Durham, NC 27706, U.S.A.

(*Received* 10 *January* 1992 *and in final form* 9 *June* 1992)

Abstract—This paper describes the water film that is formed as ice melts under a two-dimensional solid slider. The analysis is based on the contact melting theory, and accounts for the coupling between the heat transfer across the water film and the fluid mechanics of the film. The competition between pressure melting and frictional melting in the creation of the film, and the effect of slider thermal boundary conditions (isothermal vs adiabatic) are documented. The dimensionless groups that govern the film behavior are identified. The film thickness increases in the downstream direction. The water leaves the relative-motion area through the front opening and through the trailing opening. The slenderness ratio (thickness/length) of the water film depends on water properties and contact length, and is fairly insensitive to changes in the applied normal force. It is shown that if the presence of ice asperities is taken into account, the contact melting theory may anticipate the trend and order of magnitude of the coefficient of friction determined experimentally.

INTRODUCTION

FRICTION on ice has attracted considerable attention from physicists and engineers during the last 100 years. This work has been reviewed by Hobbs [1]. It is a controversial area that remains active because a purely theoretical basis for predicting the coefficient of kinetic friction is still out of reach.

There have been two main theoretical views on sliding melting and friction on ice. Reynolds [2] suggested in an essay (without any analytical backing) that the water film that separates the ice and the slider is due to pressure melting, i.e. due to the peculiar property of ice that the melting point decreases as the pressure increases (Fig. 1). Bowden and Hughes [3] offered order of magnitude calculations in support of a frictional melting (viscous dissipation) explanation for the formation of the water film. Evans *et al.* [4] contributed to this with an interface energy-balance analysis that included the effect of one-dimensional time-dependent conduction into the ice. The frictional melting view is more common today, even though additional explanations are being offered (e.g. adhesion theory [5]).

In spite of everything that has been written on pressure melting vs frictional melting, there is no analytical description of the water film, nor of the competition between pressure melting and frictional melting in the maintenance of the film. The objective of the present study is to provide this description. The analysis consists of extending to ice melting the contact melting methodology that has been developed by several authors [6–17] in the fields of heat transfer and tribology. According to the contact melting theory, the melting and sliding-friction phenomenon is due to the coupling of the heat transfer across the film, with the melting at the ice surface, and with the fluid mechanics of the water film. It is a rigorous method that accounts for changes in the direction of relative motion, i.e. along the film.

The problem of accurately predicting the coefficient of kinetic friction for skating is considerably more complicated than analyzing the continuous water film, and is beyond the objective of our study. The complications stem from the fact that most of the friction

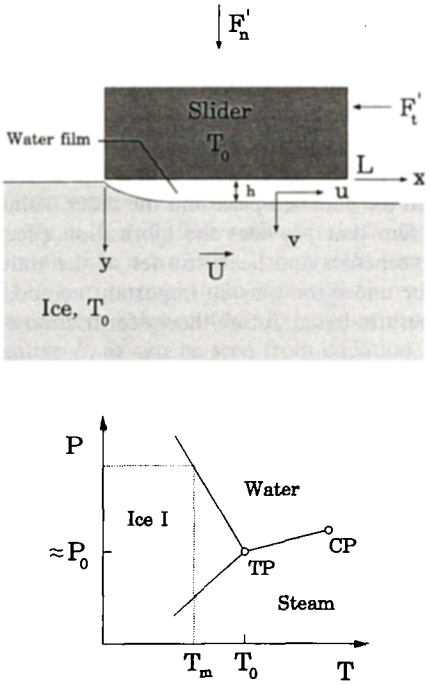

FIG. 1. Water film due to the pressure melting of ice under a slider (top), and the relationship between the melting point of ice and pressure (bottom).

NOMENCLATURE

A	constant in the linearized Clausius–Clapeyron relation, 13.6 MPa K^{-1}
B	film slenderness scale, equation (21)
B_X	B number based on X, equation (34)
c_s	specific heat of ice
C	constant of integration, equation (8)
$\tilde{C}$	dimensionless constant of integration, equation (12)
f_c	area fraction covered by contact melting
F_n	normal force
F'_n	normal force per unit length, equation (17)
$F'_{n,X}$	normal force applied on X per unit length, equation (32)
$\tilde{F}_n$	dimensionless normal force per unit length, equation (18)
$\tilde{F}_{n,X}$	$\tilde{F}_n$ number based on X and $F'_{n,X}$, equation (33)
F_t	tangential force
F'_t	tangential force per unit length, equation (19)
$\tilde{F}_t$	dimensionless tangential force per unit length, equation (20)
$F'_{t,X}$	tangential force applied on X per unit length, equation (32)
G	dimensionless function, $G = H^2$
h	water film thickness, Fig. 1
h_{sf}	latent heat of melting
k	liquid thermal conductivity
L	length of contact area, Fig. 1
N	number of asperities
P	pressure
P_0	ambient pressure
$\tilde{P}$	dimensionless excess pressure, equation (10)
Q	volumetric flow rate per unit length, equation (3)
R	pressure gradient, dP/dx
T_m	melting point
T_0	temperature of the slider and the distant ice, Fig. 1
u, v	liquid velocity components, Fig. 1
U	translational speed
x, y	Cartesian coordinates, Fig. 1
X	macroscopic length of (rough) contact area, Fig. 9.

Greek symbols

μ	viscosity
μ_f	coefficient of friction, F'_t/F'_n
ξ	dimensionless longitudinal location, x/L
ρ	density, water or ice
ϕ	viscous heating parameter, equation (25).

occurs over the small asperities that are present in the ice surface (Fig. 9). One must know the density, size, and shape of these asperities if one is to construct a conclusive theory on the coefficient of friction. On the other hand, the high-pressure sliding contact between each asperity peak and the solid slider does cause the flattening of the asperity. The pressure and friction between the flattened peak and the slider maintains a water film that provides the lubrication effect. The fluid mechanics and heat transfer of the water film must be understood, as an important component in an asperities-based, future theory for friction on ice.

WATER FILM DUE TO PRESSURE MELTING ALONE

Consider the two-dimensional configuration of Fig. 1 (top), in which a body of length L slides over the surface of a block of ice. The latter is assumed flat, i.e. without asperities. The relative motion is steady, with speed U (positive). The solid body (the slider) is pushed against the ice with the force F'_n [N m^{-1}], which is expressed per unit length in the direction normal to Fig. 1. This model is equivalent to the reverse situation in which an ice spot (asperity) of length L slides over a flat solid body. The reverse situation is a model of contact melting at the peaks of ice asperities that make contact with a solid slider (Fig. 9).

The slider and the bulk of the ice block are at the ice point $T_0 = 0°C$. The higher pressure maintained under the slider leads to the formation of a liquid film that bridges the temperature gap between the T_0 slider and the T_m melting front. Because of the anomalous behavior of water (Fig. 1, bottom), the melting front temperature falls below T_0.

The thickness of the water film, $h(x)$, can be determined by solving the Reynolds equation for the lubricating water flow

$$\frac{dP}{dx} = \mu \frac{\partial^2 u}{\partial y^2} \tag{1}$$

in conjunction with the energy equation. Integrated subject to the boundary conditions $u = 0$ at $y = 0$ and $u = U$ at $y = h$, equation (1) yields the longitudinal velocity in the water film

$$u(x,y) = \frac{1}{2\mu}(y^2 - hy)\frac{dP}{dx} + \frac{y}{h}U. \tag{2}$$

The corresponding longitudinal flow rate is

$$Q = \int_0^h u\,dy = \frac{h^3}{12\mu}\left(-\frac{dP}{dx}\right) + \frac{h}{2}U. \tag{3}$$

In the thin-film limit in which the Reynolds equation is valid, the heat transfer in the liquid film approaches pure conduction in the vertical direction [17]. In this limit the liquid temperature decreases linearly from T_0 at $y = 0$ to T_m at $y = h$. The vertical heat flux $k(T_0 - T_m)/h$ is balanced by the melting of the fresh ice that crosses the ice–water interface

$$\frac{k}{h}(T_0 - T_m) = \rho h_{sf} U \frac{dh}{dx}. \tag{4}$$

This balance is based on the assumption that the sensible cooling experienced by the approaching ice, $c_s(T_0 - T_m)$, is negligible when compared with the latent heat of melting, h_{sf}. The left-hand side of equation (4) can be expressed in terms of the local excess pressure $(P - P_0)$, by recalling the Clausius–Clapeyron relation $dP/dT_m = -A$, in which $A = -s_{sf}/v_{sf} = -h_{sf}/(T_0 v_{sf})$. In the vicinity of T_0, $A \cong 13.6$ MPa K^{-1}. Treating A as a constant, we can integrate the Clausius–Clapeyron relation in order to eliminate $(T_0 - T_m)$ from equation (4)

$$\frac{k}{Ah}(P - P_0) = \rho h_{sf} U \frac{dh}{dx}. \tag{5}$$

The conservation of mass in the liquid film region requires that

$$\frac{dQ}{dx} = U \frac{dh}{dx}. \tag{6}$$

This equation is derived easily by integrating the mass conservation equation $(\partial u/\partial x + \partial v/\partial y = 0)$ from $y = 0$ to $y = h(x)$. Integrating equation (6) in x, and introducing the constant C, we obtain

$$Q(x) = Uh(x) + C. \tag{7}$$

The problem reduces to solving equations (3), (5) and (7) for $h(x)$, $P(x)$ and $Q(x)$. First, we eliminate Q between equations (3) and (7)

$$\frac{h^3}{12\mu}\left(-\frac{dP}{dx}\right) = \frac{Uh}{2} + C. \tag{8}$$

It is convenient to introduce the following dimensionless variables:

$$\xi = \frac{x}{L}, \quad H = h\left(\frac{\mu k L^2}{\rho h_{sf} A}\right)^{-1/4} \tag{9}$$

$$\tilde{P} = \frac{P - P_0}{U}\left(\frac{k}{\rho h_{sf} A \mu}\right)^{1/2} \tag{10}$$

so that the system (5), (8) reduces to

$$\tilde{P} = H \frac{dH}{d\xi} \tag{11}$$

$$H^3\left(-\frac{d\tilde{P}}{d\xi}\right) = 6H + \tilde{C} \tag{12}$$

in which $\tilde{C}$ is the dimensionless constant that accounts for C. The boundary conditions for equations (11) and (12) are $\tilde{P} = 0$ at $\xi = 0$ and $\xi = 1$, stating that the liquid pressure matches the ambient pressure at the two ends of the liquid film. We solved equations (11) and (12) numerically by first eliminating $\tilde{P}$

$$H^3 \frac{d^2}{d\xi^2}(H^2) + 12H + 2\tilde{C} = 0. \tag{13}$$

NUMERICAL METHOD

To understand the behavior of H it is useful to rewrite equation (13) as

$$\frac{d^2 G}{d\xi^2} = -\frac{12}{G} - \frac{2\tilde{C}}{G^{3/2}} \tag{14}$$

where $G = H^2$. The conditions $\tilde{P} = 0$ at $\xi = 0$ and $\xi = 1$ in conjunction with equation (11) lead to the following boundary conditions:

$$\frac{dG}{d\xi} = 0 \quad \text{at} \quad \xi = 0 \quad \text{and} \quad \xi = 1. \tag{15}$$

Since G can never be negative, it is easy to see that the boundary conditions (15) can never be satisifed if $\tilde{C} \geqslant 0$, because the curvature $d^2G/d\xi^2$ will be negative over the entire ξ region. Similarly, although less obvious, equation (14) has only a trivial straight line solution for $\tilde{C} \leqslant -6$. The wavelengths for oscillatory behavior are too large to allow for zero slope (equation (15)) if $\tilde{C} \leqslant -6$.

Equations (14) and (15) are satisfied for any negative value of $\tilde{C}$ by the constant $G = (-\tilde{C}/6)^2$. From equation (11), however, we note that

$$\tilde{P} = \frac{1}{2}\frac{dG}{dx} \tag{16}$$

and conclude that the constant G solution (i.e. $\tilde{P} = 0$) corresponds to an unrealistic condition in which no normal force is applied to the slider.

The domain of interest corresponds to $-6 < \tilde{C} < 0$. In this domain there are three distinct solutions for every single value of $\tilde{C}$. This aspect is illustrated qualitatively in Fig. 2. The solid line indicates the only solution that is realistic. The straight line corresponds to zero normal force, as noted above. The dotted oscillatory solution $(dG/d\xi < 0)$ corresponds to a negative $\tilde{P}$, as can be seen from equation (16). This solution would be meaningful if U were negative, i.e. if the motion is reversed. The film $H(\xi)$ pro-

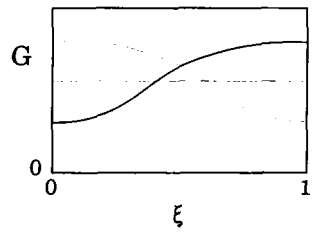

FIG. 2. The three types of $G(\xi)$ solutions of equations (14) and (15).

file that would correspond to this solution is simply the reverse (mirror image) of the $h(\xi)$ profile for positive U, which corresponds to the solid line in Fig. 2. It must also be said that in addition to the wavy solutions illustrated in Fig. 2, equations (14) and (15) admit oscillatory solutions that peak more than once in the region $0 < \xi < 1$. These solutions were ruled out because they would correspond to alternating regions of negative pressure under the slider.

Once the behavior of $G(\xi)$ was understood, it was possible to discretize equation (14), and to use the shooting method to generate a solution of the solid line type (Fig. 2). This solution was then used as the initial guess in a Newton–Raphson iteration scheme. The solution was iterated until the error in G at each node was less than 10^{-6}.

The discretization was second-order accurate, and the boundary conditions (15) were implemented using the mirror point method. The solutions proved to be stable to three decimal places using only 500 grid points; however, 2049 grid points had to be used in order to resolve graphically the steep slopes ($dG/d\xi$) for low values of $\tilde{C}$.

The integration required by the tangential force (equation (20) in the next section) was performed using the Romberg method, which was modified to accept discrete data. The convergence criterion was set at 10^{-8}. The results of the Romberg method were checked against a simple application of the trapezoidal rule over all of the grid points.

RESULTS

The dimensionless film thickness is presented in Fig. 3. The lubricating film becomes thicker toward the trailing end of the slider. Under the leading and trailing edges of the slider, the film thickness is nearly constant ($dH/d\xi = 0$ at $\xi = 0$ and $\xi = 1$; cf. equation (15)). This variation of the liquid film thickness with longitudinal position distinguishes the phenomenon of sliding by pressure melting from the corresponding phenomenon in which the melt layer is due to an imposed temperature difference [17]. In the latter, the liquid film thickness is constant. It is worth noting also that the $dH/d\xi = 0$ condition at $\xi = 0$ is not entirely visible on the curves for $\tilde{C} = -0.5$ and -1 because of the poor resolution of the drawing (i.e. the tightness of the ξ scale near $\xi = 0$).

We obtained one $H(\xi)$ curve for each value of the constant of integration $\tilde{C}$. The latter is related to the total force maintained between the slider and the ice block

$$F_n' = \int_0^L (P - P_0)\,dx \tag{17}$$

or, in dimenionless terms

$$\tilde{F}_n = \frac{F_n'}{UL}\left(\frac{k}{\rho h_{sf} A \mu}\right)^{1/2} = \int_0^1 \tilde{P}\,d\xi. \tag{18}$$

By comparing equations (18), (11) and Fig. 3 it is easy to see that F_n' is a function of $\tilde{C}$. This monotonic relationship is presented in Fig. 4. By comparing this with Fig. 3, we see that the film thickness becomes less uniform (smaller near $\xi = 0$, and larger near $\xi = 1$) as the normal force increases (or $-\tilde{C}$ decreases). At the same time, and this is somewhat surprising, the ξ-averaged value of H is fairly insensitive to the large changes in the normal force. We return to this observation in equation (21).

The net tangential force experienced by the slider is

$$F_t' = \int_0^L \mu\left(\frac{\partial u}{\partial y}\right)_{y=0} dx \tag{19}$$

or, in dimensionless terms

$$\tilde{F}_t = \frac{F_t'}{UL}\left(\frac{k}{\rho h_{sf} A \mu}\right)^{1/2} = B\int_0^1 \left(-\frac{H}{2}\frac{d\tilde{P}}{d\xi} + \frac{1}{H}\right) d\xi. \tag{20}$$

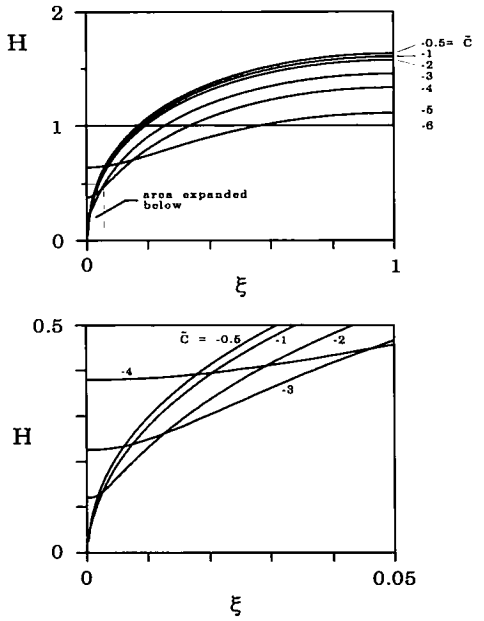

FIG. 3. The dimensionless thickness of the water film.

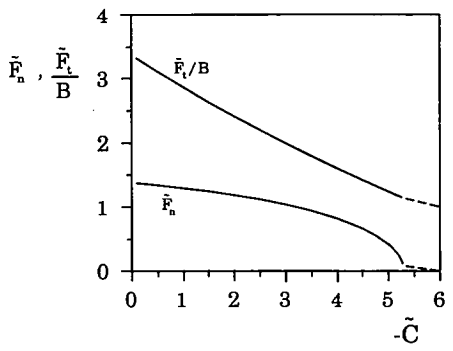

FIG. 4. The relationships of the integration constant $\tilde{C}$ with the dimensionless normal force and tangential force.

The dimensionless parameter B is much smaller than 1, because it represents the order of magnitude of the slenderness ratio of the liquid film

$$B = \left(\frac{\mu k}{\rho h_{sf} A L^2}\right)^{1/4}. \quad (21)$$

Note that the same group can be obtained by dividing by L the h scale recognized in equation (9), $(\mu k L^2/\rho h_{sf} A)^{1/4}$. It is remarkable that the slenderness scale group B depends only on water properties and the contact length L, and not on the normal force. For example, using $L = 10$ cm and the properties of saturated water at 0°C, we obtain $B \sim 7 \times 10^{-5}$.

The lack of a strong relationship between normal force and liquid film thickness is another striking difference between pressure melting and the corresponding sliding-contact melting process caused by an imposed temperature difference. In the case of melting due to a temperature difference, the film thickness varies as the normal force raised to the power $-1/3$; in other words, it decreases sensibly as the normal force increases (ref. [17], equation (17)).

Figure 4 also shows the group $\tilde{F}_t/B$ as a function of the abscissa parameter $-\tilde{C}$. Since the only solution for $\tilde{C} = -6$ is known to be a straight line at $H = 1$, $\tilde{F}_n$ and $\tilde{F}_t/B$ can be calculated analytically. They are 0 and 1, respectively. As $\tilde{C}$ approaches -6, however, an oscillatory solution which is distinct from the straight line trivial solution becomes hard to find due to the small amplitude of the oscillations. As many as 10 000 grid points were used to pick up solutions for $\tilde{C} < -5$. The dotted lines represent the connection between the last numerically determined solution and the known analytical solution at $\tilde{C} = -6$.

By eliminating $\tilde{C}$ between the two curves of Fig. 4 we obtain the upper graph of Fig. 5 (the solid line, $\phi = 0$, where ϕ will be defined in equation (25)), which shows the relationship between the tangential force and the applied normal force. As expected, the tangential force increases monotonically as the normal force increases. Since both $\tilde{F}_t/B$ and $\tilde{F}_n$ are of order 1 in this upper graph, we conclude that the smallness of $\tilde{F}_t$ (or F'_t) relative to $\tilde{F}_n$ (or F'_n) is governed by the film slenderness scale B.

This conclusion is emphasized in the lower part of Fig. 5 (the solid line), on the ordinate of which we see the group $(\tilde{F}_t/\tilde{F}_n)/B$. Recall that the ratio $\tilde{F}_t/\tilde{F}_n = F'_t/F'_n$ is the friction coefficient, and note that for dimensionless normal forces of order 1 the ordinate group is nearly constant (approximately equal to 2). This means that when $\tilde{F}_n \sim O(1)$, the friction coefficient is approximately $2B$, i.e. a number of order 10^{-4} when $L = 10$ cm. However, in order for $\tilde{F}_n$ to be of order 1, the actual normal force per unit speed (F'_n/U) must be of order 10^5 (N m^{-1})/(m s^{-1}).

There are clearly two conditions that would lead to this regime of very high F'_n/U values: high F'_n or small U. In situations of very small U, however, the assumption of no vertical velocity—an assumption

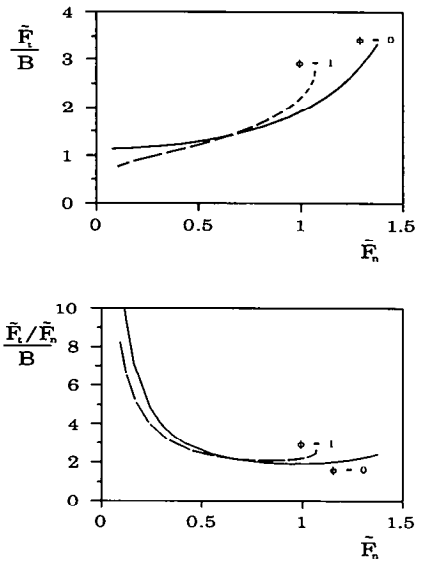

FIG. 5. The relationship between the tangential force, the normal force and the film slenderness scale B. The lower graph shows the friction coefficient $\tilde{F}_t/\tilde{F}_n$. The dashed lines show the effect of viscous heating in the film (isothermal slider).

that is implicit in equation (4)—becomes suspect. Objects moving very slowly in the horizontal direction might begin to sink into the ice [18, 19]. Conditions under which the friction coefficient is $2B$, therefore, are those in which very heavy objects slide over ice at finite velocities.

Figures 4 and 5 (the lower graph) show that as the normal force decreases to the limit where $-\tilde{C} = 6$, the friction coefficient $\tilde{F}_t/\tilde{F}_n$ tends to infinity. This unrealistic limit is due to the way in which the analysis was set up; specifically, to the assumption that a liquid film covers the entire length L even as the normal force approaches zero. We had to make this assumption to invoke pressure conditions at the inlet and the outlet of the relative motion gap. Because of this assumption, the tangential force tends to a finite value in the limit of zero normal force. Future studies may consider refining the present theory by allowing for the disappearance of liquid in the inlet region as the normal force decreases.

COMPARISON WITH EXPERIMENTAL MEASUREMENTS

We were unable to find any experimental work in the regime of extremely high normal forces, which is hardly surprising. Figure 6, however, shows a comparison with the experimental work of Oksanen and Keinonen [20]. These authors measured the coefficient of friction for ice sliding on ice at a variety of speeds and normal loads. This set of measurements was better suited for comparison with our predictions than other published experimental results—e.g. Bowden and Hughes [3] or Evans *et al.* [4]—because Oksanen

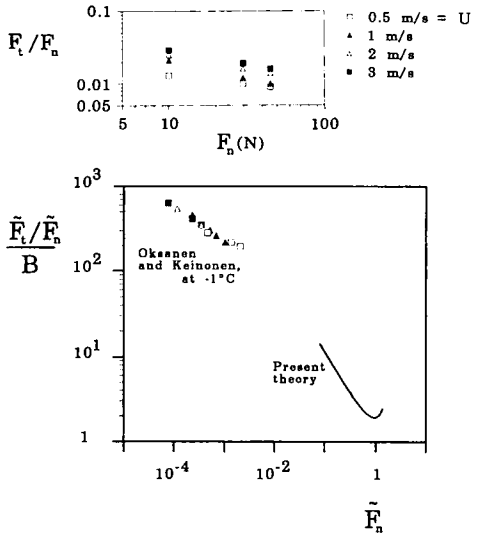

FIG. 6. Comparison of experimental data with theoretical results. The insert shows the original (dimensional) experimental data.

and Keinonen varied both the normal load and sliding speed at three different temperatures, including $-1°C$. Our analysis is based on the assumption that the ice is not subcooled.

In plotting the data we have assumed that the ice surfaces are perfectly smooth, i.e. that the length X of the macroscopic contact area is the same as the water film length L. The effect of ice asperities on the plotting of the experimental data, and the good agreement with theory, is discussed in the concluding section of the paper.

It is encouraging that our results qualitatively agree with experiment: extension of our theoretical curve into the regime of the experimental forces agrees in an order of magnitude sense with the experimental values. That our curve does not quite predict the slope of the curve in the experimental regime is understandable. Our model relies upon the existence of fluid at the leading edge of the slider. This fluid layer at the leading edge can only be present if the pressures are such that fluid is actually forced out in front of the slider. In the experimental regime the pressures are not nearly high enough for that.

More significant, moreover, is the monotonic relationship between the coefficient of friction and the dimensionless normal force that the experimental data indicate. These data represent measurements made at four different velocities and three different normal loads. The insert in Fig. 6 shows Oksanen and Keinonen's data, before nondimensionalization. The straight line the data form once they have been transformed in our dimensionless parameters suggests that our normal force $\tilde{F}_n$ is the appropriate dimensionless group for analyzing skating at temperatures near the melting point, even in low force regimes. Oksanen and Keinonen's results for sliding on subcooled ice (i.e. below $-1°C$) did not form straight lines after transformation, indicating that our dimensionless force—which we derived while assuming the ice was not subcooled—is not an appropriate non-dimensionalization for sliding on subcooled ice.

WATER FILM DUE TO PRESSURE MELTING AND VISCOUS DISSIPATION

We turn our attention to the limit in which the relative motion is sufficiently fast so that the viscous shearing of the liquid film generates enough heat to alter the pressure melting process discussed until now. The velocity distribution in the liquid and the flow rate continue to be described by equations (2) and (3). What changes is the energy equation for the liquid, which now contains the viscous heating effect as a source term

$$0 = k\frac{\partial^2 T}{\partial y^2} + \mu\left(\frac{\partial u}{\partial y}\right)^2. \tag{22}$$

This equation has been simplified in accordance with the thin-film limit discussed above (equation (4)). It states that the liquid temperature is generally two-dimensional, $T(x, y)$, because the longitudinal velocity distribution is two-dimensional, $u(x, y)$. The transfer of heat proceeds vertically by conduction, and it involves the rejection (to $y = h$, or $y = 0$, or both) of the frictional volumetric heating rate $\mu(\partial u/\partial y)^2$.

Equation (22) can be integrated twice in y, after estimating $\partial u/\partial y$ based on equation (2). The resulting expression for T is omitted for the sake of conciseness. It contains two 'constants' of integration, which are in fact functions of x. These are determined by invoking the two boundary conditions in the transversal direction, one at the melting front, $T = T_m(x)$ at $y = h$, and the other at the slider surface ($y = 0$). As far as the slider surface condition is concerned, we consider the following two extremes.

Isothermal (high conductivity) slider

In the limit in which the slider material approaches a perfect thermal conductor, the slider surface is isothermal and the $y = 0$ boundary condition is $T = T_0$. The resulting expression for the temperature distribution in the liquid film is

$$T - T_m = \frac{R^2}{24\mu k}(h^4 - 3h^2y^2 + 4hy^3 - 2y^4) + \frac{RU}{6k}\left(3y^2 - 2\frac{y^3}{h} - h^2\right) + \frac{\mu U^2}{2k}\left(1 - \frac{y^2}{h^2}\right) + \left[\frac{1}{h}(T_m - T_0) + \frac{R^2h^3}{24\mu k} - \frac{RUh}{6k} + \frac{\mu U^2}{2hk}\right](y - h) \tag{23}$$

where R is shorthand for the pressure gradient, $R = dP/dx$.

Beyond this point, the analysis follows the steps

outlined between equations (4) and (12). It begins with replacing the left-hand side of equation (4) with the actual heat flux ($-k\,\partial T/\partial y$, at $y = h$) calculated based on equation (22). It then relies on the linearized Clausius–Clapeyron relation to couple the melting point $T_m(x)$ to the local pressure in the film $P(x)$, recognizes the conservation of mass (6), and the non-dimensional variables defined by equations (9) and (10). In the end, equation (12) remains intact, while equation (11) assumes the new form

$$\tilde{P} - H\frac{dH}{d\xi} + \frac{\phi}{6}\left[H^2\frac{dP}{d\xi} + \frac{H^4}{4}\left(\frac{dP}{d\xi}\right)^2 + 3\right] = 0 \quad (24)$$

where ϕ is a dimensionless viscous heating parameter

$$\phi = U\left(\frac{\mu A}{\rho h_{sf} k}\right)^{1/2}. \quad (25)$$

By using the properties of water at 0°C, we find that $\phi = U \times 0.011\ \text{s m}^{-1}$, meaning that ϕ exceeds the order of 1 when U becomes greater than 100 m s^{-1}. If we compare equations (24) and (11) we see that the sliding due to pressure melting alone (the first part of this study) represents the $\phi \to 0$ limit of the more general problem considered in this section.

Finally, by eliminating $\tilde{P}$ between equations (12) and (24) we obtain

$$H^3\frac{d^2(H^2)}{d\xi^2} + 12H + 2\tilde{C} + \frac{\phi}{6}(4\tilde{C}H + \tilde{C}^2)\frac{dH}{d\xi} = 0 \quad (26)$$

which replaces equation (13). This was solved subject to the end conditions $\tilde{P} = 0$, which means that

$$\frac{dH}{d\xi} = \phi\left(\frac{1}{H} + \frac{\tilde{C}}{3H^2} + \frac{\tilde{C}^2}{24H^3}\right) \quad (27)$$

at $\xi = 0, 1$. As in the first part of the paper, the numerical procedure led to a parametric solution in terms of the constant $\tilde{C}$. Other numerical details are given in the next section. The $\tilde{C}$ parameter was then eliminated, and the number of graphs reduced so that the results can be presented directly in terms of the physical input variables, $\tilde{F}_n$ and ϕ. Figure 7 shows that in the range $\phi = 0$–1 the frictional heating generated by the film has a negligible effect on the thickness (size, shape) of the water film. The same can be said about the effect of viscous heating on the friction coefficient. The dash curves projected in Fig. 5 show the small effect that ϕ has on the tangential force and the friction coefficient.

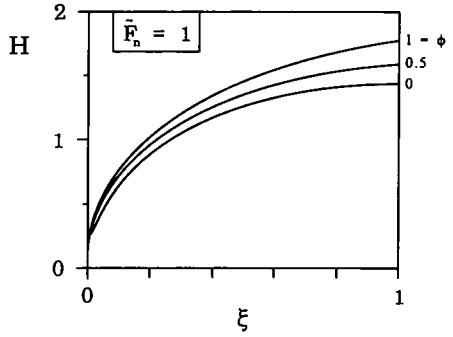

FIG. 7. The effect of viscous heating on the water film thickness (isothermal slider, $\tilde{F}_n = 1$).

Adiabatic (low conductivity) slider

In the opposite extreme, where the slider material is a poor conductor, we can model the slider surface as adiabatic, $\partial T/\partial y = 0$ at $y = 0$. The resulting expression for the temperature distribution $T(x, y)$ in the liquid film is omitted because it is the same as equation (26) in ref. [14], although in the present case T_m is a function of x. For the heat flux that arrives at the melting front (and replaces the left-hand side of equation (4)) this $T(x, y)$ expression yields

$$-k\left(\frac{\partial T}{\partial y}\right)_{y=h} = \frac{h^3}{12\mu}\left(\frac{dP}{dx}\right)^2 + \frac{\mu U^2}{h}. \quad (28)$$

By repeating the steps between equations (4) and (12), we arrive again at equation (12) and, in place of equation (11), at

$$\frac{dH}{d\xi} = \phi\left[\frac{H^3}{12}\left(\frac{d\tilde{P}}{d\xi}\right)^2 + \frac{1}{H}\right]. \quad (29)$$

Numerical results we obtained by first eliminating $\tilde{P}$ between equations (12) and (28)

$$\frac{dH}{d\xi} = \phi\left(\frac{4}{H} + \frac{\tilde{C}}{2H^2} + \frac{\tilde{C}^2}{12H^3}\right) \quad (30)$$

and imposing the integral condition

$$\int_0^1 \frac{dP}{d\xi}\,d\xi = 0. \quad (31)$$

For both the isothermal and adiabatic sliders a shooting method was used. In the isothermal case, central differences were used except at the boundaries. Since central differencing of equation (26) results in a nonlinear equation for the value of the unknown grid point, each step was iterated until the change in consecutive iterative values became less than 10^{-5}. Similarly, the entire process was repeated until the boundary conditions were satisfied to within 1×10^{-5}.

For the adiabatic slider, central differences resulted in numerical instability in the form of bounded oscillations. First-order accurate noncentered differences were therefore used and smooth solutions were achieved. In both cases, integration to find forces and pressures was performed using the trapezoidal rule. Grid refinement showed that 2000 grid points were sufficient to get values for F_n' and F_t' that were stable to within 1%.

The results for the friction coefficient ($\tilde{F}_t/\tilde{F}_n$) are

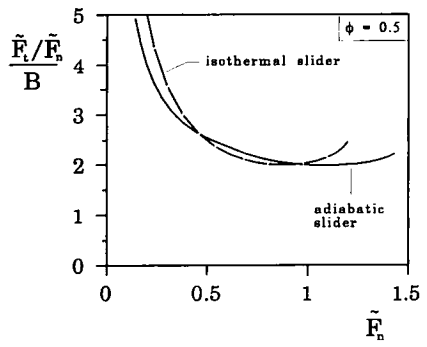

FIG. 8. The effect of the slider thermal boundary condition on the friction coefficient ($\phi = 0.5$).

reported in Fig. 8 (the solid line) for a given speed, $\phi = 0.5$. The dashed line corresponds to the isothermal slider solution discussed in the preceding section, and shows that the character of thermal boundary condition at the slider surface has a negligible effect on the calculated results. By recalling the negligible effect that was indicated by the dashed lines in Fig. 7, we conclude one more time that the viscous heating of the water film is a minor effect next to pressure melting in this regime of large normal forces, where F_n'/U is of order 10^5 (N m^{-1})/(m s^{-1}).

An interesting feature of the adiabatic slider model is that all the melting is due to the frictional heating of the liquid film. This means that when the viscous dissipation effect becomes sufficiently small ($\phi \to 0$) the liquid film vanishes. In that limit, no 'pressure melting' occurs under the adiabatic slider regardless of the size of the imposed normal force. When the slider surface is adiabatic and viscous dissipation is negligible, the local slider temperature matches (drops to) the local melting front temperature, and the vertical temperature difference across the film becomes zero. The film vanishes because there is no heating effect (vertical temperature gradient) to sustain it.

CONCLUDING REMARKS: THE EFFECT OF ICE ASPERITIES

In this paper we determind analytically and numerically the shape and properties of the water film between slider and ice. The method was the same as in earlier contact melting studies of regular substances [6–17]: at every x, the fluid mechanics of the film were coupled to the heat transfer across the film. The analysis revealed the proper dimensionless groups that govern the existence of the water film, and the relative importance of pressure and frictional effects in maintaining (feeding) the film. Specific conclusions were drawn at the end of each section that contained results.

The main conclusion is that the applied normal force must be sufficiently large, or the individual asperities sufficiently rare and small, for the water film to cover the contact length L entirely. This requirement is summarized in the dimensionless group $\tilde{F}_n$, which must be of order 1 (Figs. 5 and 8) if the water film is to flow out of the relative motion gap through the front opening ($x = 0$) and through the trailing opening ($x = L$).

The water film described in this paper is a step toward a theoretical understanding of friction on ice. For example, we can apply the present results to a single ice asperity of swept length L, average pressure F_n'/L, and average shear stress F_t'/L. While it is true that the real asperity does not have the two-dimensional shape assumed in Fig. 1—a better model for its flattened peak would be a disc of diameter L—the present results for friction coefficient agree within 50% with the value reported in this paper for the two-dimensional contact area (this level of agreement was demonstrated in the analysis of sliding contact melting over regular substances [17]).

Let X be the macroscopic length of the rough ice surface (Fig. 9). Assume further that the number of asperities over X is N. The coefficient of friction for the individual asperity ($\mu_f = F_t'/F_n'$) is the same as the apparent coefficient of friction for the X-long rough surface ($NF_t'/NF_n' = \mu_f$). The total forces applied over the entire (rough) surface are

$$F_{n,X}' = NF_n' \quad \text{and} \quad F_{t,X}' = NF_t'. \tag{32}$$

We can now return to Fig. 6 and recognize the solid curve in the lower right-hand corner as the theory for the coefficient of friction μ_f. That curve was plotted in terms of dimensionless coordinates based on the asperity length L (note that B varies as $L^{-1/2}$). The experimental data have been plotted on the same graph by assuming that the macroscopic surface is perfectly smooth, which is the same as replacing X with L.

Consider now the possibility (certainty) that asperities were present in the experiment. This means that

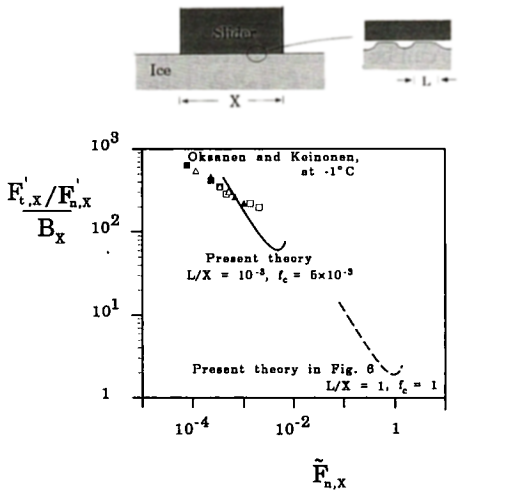

FIG. 9. The effect of the ice asperity length on the agreement between the contact melting theory and experimental coefficient of friction measurements.

the asperity length L (unknown) that should have been used in nondimensionalizing the data was much smaller than the macroscopic length X. The information of Fig. 6 can be replotted in Fig. 9 by using the known length X of the rough surface as the length scale, and the actual (measured) forces $F'_{n,X}$ and $F'_{t,X}$

$$\tilde{F}_{n,X} = \frac{F'_{n,X}}{UX(\rho h_{sf} A \mu/k)^{1/2}} \tag{33}$$

$$B_X = \left(\frac{\mu k}{\rho h_{sf} A X^2}\right)^{1/4}. \tag{34}$$

Figure 9 shows that in terms of the new dimensionless coordinates $\tilde{F}_{n,X}$ and $F'_{t,X}/F'_{n,X}/B_X$ (or μ_f/B_X), the theory is represented by a family of curves according to two additional parameters, the length ratio L/X and the fraction of X that is associated with contact melting

$$f_c = \frac{NL}{X}. \tag{35}$$

From this entire family, the curve that resembles the cluster of experimental data has an L/X ratio of order 10^{-3}, and a contact melting area fraction f_c of order 5×10^{-3}. Future experimental studies may consider the question of whether these L/X and f_c values are supported by actual measurements. The L/X value of 10^{-3} would correspond to flattened asperities of length $L \sim 0.2$ mm in the experiment of Oksanen and Keinonen [20].

In conclusion, in order to anticipate the coefficient of friction, one must know not only the contact melting results developed in this study but also the size and density of ice asperities.

REFERENCES

1. P. V. Hobbs, *Ice Physics*, pp. 411–421. Oxford University Press (1974).
2. O. Reynolds, *Papers on Mechanical and Physical Subjects*, Vol. 2, pp. 734–738. Cambridge University Press (1901).
3. F. P. Bowden and T. P. Hughes, The mechanism of sliding on ice and snow, *Proc. R. Soc. Math. Phys. Sci.* **172,** 280–298 (1939).
4. D. C. B. Evans, J. F. Nye and K. J. Chesseman, The kinetic friction of ice, *Proc. R. Soc. Lond. A* **347,** 493–512 (1976).
5. K. Tusima, Friction of a steel ball on a single crystal of ice, *J. Glaciol.* **19,** 225–235 (1977).
6. W. R. D. Wilson, Lubrication by melting a solid, *J. Lubrication Technol.* **98,** 22–26 (1976).
7. V. Bicego, A. Figari and G. Poletti, Lubrication of a melting slider under nonisothermal conditions, *J. Lubrication Technol.* **103,** 436–442 (1981).
8. F. E. Moore and Y. Bayazitoglu, Melting within a spherical enclosure, *J. Heat Transfer* **104,** 19–23 (1982).
9. S. H. Emerman and D. L. Turcotte, Stokes' problem with melting, *Int. J. Heat Mass Transfer* **26,** 1625–1630 (1983).
10. A. K. Stiffler, Friction and wear with a fully melting surface, *J. Tribol.* **106,** 416–419 (1984).
11. M. Bareiss and H. Beer, An analytical solution of the heat transfer process during melting of an unfixed solid phase change material inside a horizontal tube, *Int. J. Heat Mass Transfer* **27,** 739–746 (1984).
12. M. K. Moallemi and R. Viskanta, Melting around a migrating heat source, *J. Heat Transfer* **107,** 451–458 (1985).
13. M. K. Moallemi and R. Viskanta, Experiments on fluid flow induced by melting around a migrating heat source, *J. Fluid Mech.* **157,** 35–51 (1985).
14. M. K. Moallemi, B. W. Webb and R. Viskanta, An experimental and analytical study of close-contact melting, *J. Heat Transfer* **108,** 894–899 (1986).
15. S. K. Roy and S. Sengupta, The melting process within spherical enclosures, *J. Heat Transfer* **109,** 460–462 (1987).
16. B. W. Webb, M. K. Moallemi and R. Viskanta, Experiments on melting of unfixed ice in a horizontal cylindrical capsule, *J. Heat Transfer* **109,** 454–459 (1987).
17. A. Bejan, The fundamentals of sliding contact melting and friction, *J. Heat Transfer* **111,** 13–20 (1989).
18. A. Bejan and P. A. Tyvand, The pressure melting of ice under a body with flat base, *J. Heat Transfer* **114,** 529–531 (1992).
19. P. A. Tyvand and A. Bejan, The pressure melting of ice due to an embedded cylinder, *J. Heat Transfer* **114,** 532–535 (1992).
20. P. Oksanen and J. Keinonen, The mechanism of friction of ice, *Wear* **78,** 315–324 (1982).